Integrated Isolated OBC for EVs with 6-phase Traction Motor Drives

Integrated Isolated OBC for EVs with 6-phase Traction Motor Drives

Paolo Pescetto
Department of Energy Galileo Ferraris
Politecnico di Torino, Torino, Italy
paolo.pescetto@polito.it

Gianmario Pellegrino
Department of Energy Galileo Ferraris
Politecnico di Torino, Torino, Italy
gianmario.pellegrino@polito.it

***Abstract*—This work deals with a new topology of on-board integrated battery charger intended for road electric vehicles equipped with a 6-phase traction motor drive. The proposed OBC topology deeply integrates the battery charger within the e-drive powertrain, thus reducing cost and volume of the charger respect to non-integrated solutions. Moreover, galvanic insulation is provided, differently from all fully integrated charger in the literature. Finally, the charger has embedded PFC capability, so the AC grid current is absorbed at unitary power factor and low THD. Extensive simulation results show the feasibility of the proposed solution.**

***Index Terms*—On board charger, multiphase synchronous motor, electric vehicle, integrated OBC, PFC, multiphase machine, multi three-phase machine.**

I. Introduction

The market of Electric Vehicles (EVs) is rapidly growing in the last decade, both for economical and environmental benefits. This trend imposes relevant technology challenges and therefore it is pushing the academic and industrial research toward innovative solutions [1]. This includes evolution in motor design and control strategy, power converters, new battery technologies and charging solutions. On the motor design side, growing power ratings are pushing the introduction of multi-three phase drives, for increased system reliability and reduced phase current rating. In particular, the adoption of 6-phase motors has been rapidly growing in the last years [2], [3].

Dealing with battery charging, the research focuses on fast-charging stations and On-board Battery Chargers (OBC). The modern fast-charging stations are normally equipped with high power rectifier with Power Factor Correction (PFC) and isolated DC/DC converter, permitting a recharge power of the order of 100 kW or more. Complementary to the use of fast charging stations, most of the EVs are equipped with OBC for low (3-6 kW) or medium (10-20 kW) power overnight charging [4].

An OBC can be developed according to two main approaches, nominally stand-alone and integrated solutions. The latter is by definition more compact, exploiting the EV motor as passive element and its inverter for energy conversion. Anyway, most of the integrated OBC in the literature [5]–[8] and automotive industry [9] are designed for 3-phase motors and are not compatible with multi-three phase machines. Moreover, unless an additional isolation stage is added, none of the reported integrated solutions provides galvanic insulation between grid and battery [10]–[12], commonly guaranteed by stand-alone OBCs and required by most of car makers. Finally, some of the solutions proposed in the literature produce torque at the shaft during charging, which may cause vibration and need for rotor locking.

This work proposes an innovative OBC integrated with a 6-phase synchronous motor drive designed for EV traction applications, providing galvanic insulation between the grid and the vehicle battery and with embedded PFC capability. Finally, differently from many other topologies, the proposed OBC is bidirectional, thus permitting Vehicle to Grid (V2G) operation. Dedicated control strategies were developed for regulating the charging power, the grid current Power Factor (PF) and THD and maintaining zero shaft torque. Comprehensive simulation results prove the feasibility of the proposed solution and its performance.

II. EV Under Test

The ratings of the EV traction drive under test and battery are reported in Table I. The motor is an automotive internal PM Synchronous Machine (PMSM) equipped with NdFeB permanent magnets and presenting two symmetric three-phase sets of stator windings [13], [14], indicated with the subscripts 1 and 2. Each winding set is fed by a standard 2-level 3-phase inverter, called INV.1 and INV.2. The topology of the drive during traction mode is reported in Figure 1.

It is worth noticing that the two 3-phase sets and inverters are identical. Therefore, every topology and solution proposed in this work can be equivalently applied reversing the sets 1 and 2.

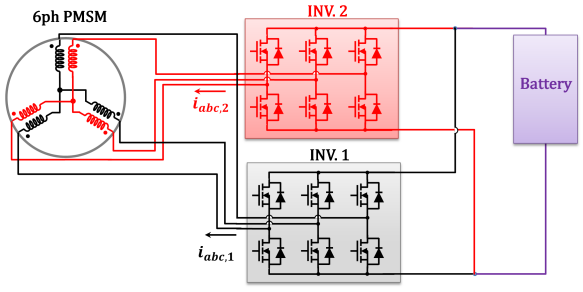

Fig. 1. Six-phase traction e-drive

TABLE I
RATINGS OF THE TRACTION DRIVE.

motor		
rated power	67	kW
rated torque	80	Nm
base speed	≈5500	rpm
max speed	≈12000	rpm
pole pairs	3	
inverter		
max phase current	235	Arms
DC voltage	800	V
switching frequency	12÷50	kHz

The traction drive presents a motor designed for 800 V DC-bus. The flux maps of the motor under test are reported in Figure 2. Similarly to most of the traction motors for EVs, the machine under test is designed to reach high base and maximum speed. Therefore, the machine inductance is in the order of magnitude of a few mH.

The considered EV application and standard [15] impose the specifications and constrains for the integrated OBC:

- limited or possibly no additional hardware should be added to the vehicle out of the drive itself
- galvanic isolation between the battery and the power grid
- possibility to interconnect with 1-phase or 3-phase grid (max charging power 6.7 kW and 11 kW respectively)
- capability of charging the battery either in Constant Voltage (CV) or Constant Current (CC) modes
- grid current THD $<$ 5% and PF$>$0.95
- no torque production, movement or thermal stress of the motor during charging
- Vehicle to Grid (V2G) capability.

Additionally, it is possible that in the future the Transmission System Operator (TSO) may require to the EVs to contribute to regulating the grid reactive power [16]. In this case, the the OBC should be able to impose the desired PF$<$1, still with minimum harmonic distortion.

III. MODELING OF THE DUAL 3-PHASE PMSM

This section briefly reports the equations adopted to model the dual 3-phase PMSM. Bold symbols represent vector quantities. The subscripts 1 and 2 refer to the first and second 3-phase set, while if the subscript number is missing the quantity refers to the magnetizing component. The d axis is defined as the direction of PM magnetization.

Exploiting the rotor dq reference frame, the voltage in each 3-phase set $\boldsymbol{v_{dq,1}}$ and $\boldsymbol{v_{dq,2}}$ can be computed as:

$$\boldsymbol{v_{dq,1}} = R_s \boldsymbol{i_{dq,1}} + \frac{\mathrm{d}\boldsymbol{\lambda_{dq,1}}}{\mathrm{d}t} + \mathbf{J}\omega\boldsymbol{\lambda_{dq,1}} \tag{1}$$

$$\boldsymbol{v_{dq,2}} = R_s \boldsymbol{i_{dq,2}} + \frac{\mathrm{d}\boldsymbol{\lambda_{dq,2}}}{\mathrm{d}t} + \mathbf{J}\omega\boldsymbol{\lambda_{dq,2}} \tag{2}$$

where R_s is the stator resistance, ω is the electrical angular frequency and $\mathbf{J} = \begin{bmatrix} 0 & -1 \\ 1 & 0 \end{bmatrix}$ is the complex operator matrix.

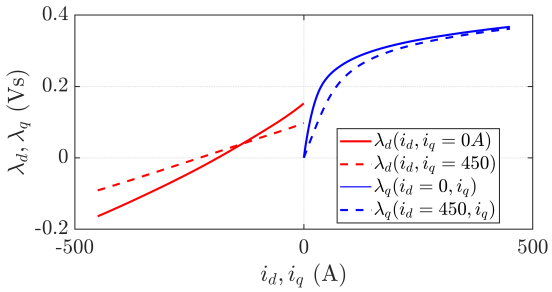

Fig. 2. Saturation flux maps of the motor under test.

The flux linkage in each 3-phase set depends on each of the 6 phase currents. Due to magnetic saturation, the current-to-flux characteristic is highly non-linear:

$$\begin{cases} \boldsymbol{\lambda_{dq,1}} = \boldsymbol{\lambda_{dq,1}}\left(\boldsymbol{i_{dq,1}}, \boldsymbol{i_{dq,2}}\right) \\ \boldsymbol{\lambda_{dq,2}} = \boldsymbol{\lambda_{dq,2}}\left(\boldsymbol{i_{dq,1}}, \boldsymbol{i_{dq,2}}\right) \end{cases} \tag{3}$$

Considering the sign of the currents as in Figure 1, the magnetizing current $\boldsymbol{i_{dq}}$ is defined as:

$$\boldsymbol{i_{dq}} = \boldsymbol{i_{dq,1}} + \boldsymbol{i_{dq,2}} \tag{4}$$

Similarly to a transformer, the flux linkage in each 3-phase set is given by a magnetizing component plus a leakage flux:

$$\boldsymbol{\lambda_{dq,1}} = \boldsymbol{\lambda_{dq}} + L_\sigma \boldsymbol{i_{dq,1}} \tag{5}$$

$$\boldsymbol{\lambda_{dq,2}} = \boldsymbol{\lambda_{dq}} + L_\sigma \boldsymbol{i_{dq,2}} \tag{6}$$

where L_σ is the leakage inductance. The magnetizing flux is retrieved from the common mode flux and current:

$$\boldsymbol{\lambda_{dq}} = \frac{\boldsymbol{\lambda_{dq,1}} + \boldsymbol{\lambda_{dq,2}}}{2} - L_\sigma \frac{\boldsymbol{i_{dq,1}} + \boldsymbol{i_{dq,2}}}{2} \tag{7}$$

The relationship between $\boldsymbol{i_{dq}}$ and $\boldsymbol{\lambda_{dq}}$ is given by the flux maps in Figure 2. The motor torque can be computed as:

$$T = \frac{3}{2} p \left(\lambda_d i_q - \lambda_q i_d\right) \tag{8}$$

IV. GENERAL CONCEPT OF IFI-OBC

The concept of the proposed Isolated Fully-Integrated On-board Battery Charger (IFI-OBC) is to use the 6-phase PMSM as an isolation transformer and the inverter for energy conversion. This is proposed both for single- or 3-phase AC main input, obtaining the topologies named IFI-1ph and IFI-3ph respectively. Particular focus will be given to the IFI-1ph case.

The main advantage of the proposed solutions is that they do not require additional electrical hardware respect to the drive itself. The grid outlet is directly connected to the motor phases without line filters. Moreover, a good power quality of the grid current is achieved. The proposed integrated battery charger is bidirectional, so V2G operation is also possible.

The main issue is that, since the primary winding of the equivalent transformer is directly connected to the grid, the amplitude of the magnetizing flux is determined by the grid

voltage amplitude and frequency. Considering a phase voltage of 230 Vrms @ 50 Hz, the resulting peak flux amplitude is approximately 1 Vs, which is too high for the PMSM under test (see Figure 2). Therefore, the proposed IFI-OBC is applicable assuming the motor windings can be reconfigured to increase the number of turns during charging. If the number of turns is increased by a factor n, the magnetizing flux and current λ'_{dq} and i'_{dq} in the reconfigured machine will be:

$$\boldsymbol{\lambda'_{dq}} = n \cdot \boldsymbol{\lambda_{dq}} \quad \boldsymbol{i'_{dq}} = \frac{1}{n} \cdot \boldsymbol{i_{dq}} \tag{9}$$

The reconfiguration can be obtained, as an example, by changing the connection of the pole pairs from parallel to series. Since the machine under test presents 3 pole pairs, in the following we will assume $n = 3$.

V. 3-phase Input OBC (IFI-3ph)

The proposed topology for IFI-3ph is presented in Figure 3(a). One of the two inverter units (INV.1 in the Figure) is disconnected and not used. The motor terminals of the correspondent 3-phase set are then connected to the grid.

In this way, the first 3-phase set acts as the primary winding of an equivalent isolation transformer, with the grid imposing a rotating excitation field to the PMSM. Since the two 3-phase sets are magnetically coupled, the magnetizing flux imposed by the grid is linked also to the second 3-phase set of the PMSM, which behaves as the secondary winding of the equivalent transformer.

The INV.2 is controlled to impose the 3-phase grid current (Figure 3(b)). The grid dq coordinates are exploited, being the grid position θ_g defined by the phase of $v_{g,a}$. The reference current $i^*_{g,d}$ determines the absorbed grid power while the PF depends on $i^*_{g,q}$. In normal conditions, the PF should be as high as possible ($i^*_{g,q} = 0$, PF≈1). A different phase shift

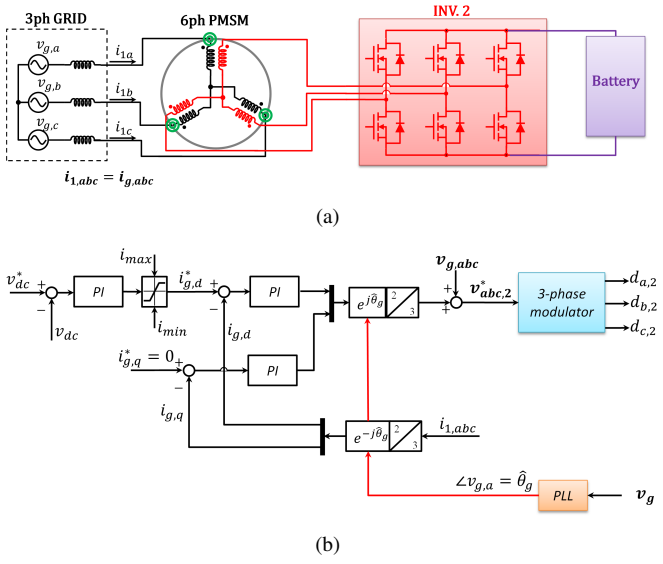

Fig. 3. Proposed IFI-3ph OBC (a) topology (b) control block diagram. The d, g and q, g components refer to grid coordinates.

between grid current and voltage may be imposed if required by the TSO for reactive power regulation. V2G operation is also possible, since each element of the system is bidirectional.

The main concern about the IFI-3ph OBC solution is that the rotating magnetic flux produces pulsating torque at two times the grid frequency. This requires a rotor locking mechanism and accepting mechanical stress of the shaft and bearings during overnight charge. The solution of this issue is currently under investigation, so the IFI-3ph configuration will not be further discussed here.

VI. 1-phase Input OBC (IFI-1ph)

The IFI-1ph OBC is presented in two versions, reported in Figure 4(a) and Figure 4(b). The first one will be referred to as "base" IFI-1ph, while the second includes an active zero torque control.

The base topology IFI-1ph OBC (Figure 4(a)) is formally similar to the IFI-3ph case. With reference to the traction drive of Figure 1, INV.1 is disconnected, while the output of two phases (b_1 and c_1 in the figure) of the same 3-phase set are connected to the grid terminals. The third phase is open. On the second 3-phase set, the winding connections are not modified. In this case, two phases only are used while the third one is disabled by opening the correspondent switches of INV.2.

The grid imposes a sinusoidal voltage excitation between the phases b_1 and c_1, producing a pulsating flux in $\alpha\beta$ coordinates. Since the two 3-phase sets are magnetically coupled, such pulsating flux is linked to the phases b_2 and c_2. Again, the PMSM works as an insulating transformer, exploiting the magnetic coupling between the phases of the different sets. The control of the grid current will be detailed in Section VI-A.

As said, the OBC should not produce torque during charging. Two alternative solutions are proposed for obtaining zero torque, described in Sections VI-B and VI-C. In both cases, $T = 0$ is obtained by forcing the magnetizing flux $\boldsymbol{\lambda_{dq}}$ to be in d axis, i.e. aligned with the PM.

A. Power Factor Correction Control

For regulating the grid current, the legs b_2 and c_2 of INV.2 are controlled as an H-bridge through a non-conventional current loop. As shown in Figure 5, the controlled variable is the grid current i_g, i.e. the current in the primary side of the equivalent transformer. Such current is flowing through the phases b_1 and c_1. The output of the PI regulator, enhanced by a feed-forward of v_g, is the voltage imposed in the battery side, i.e. the voltage $v_{bc,2}$ between the phases b_2 and c_2.

Since the inverter switching frequency (12 to 50 kHz) is much higher than the grid frequency (50 Hz), a PI regulator is normally sufficient for accurate control of i_g. If needed, a resonant controller can be adopted instead. A standard H-bridge modulator is adopted to convert the voltage reference v^*_{bc2} into the proper gate signal of the legs b_2 and c_2.

An external voltage loop sets the reference amplitude of i^*_g in order to obtain the desired voltage at the battery terminals. The reference v^*_{dc} is compared with the measured value v_{dc} and the discrepancy is input to a PI regulator, whose output

is saturated at the maximum charging current amplitude. This permits to control the charging process either in CC (for low battery SOC) or CV (for high SOC) mode.

The phase of the grid voltage is extracted by a Phase Locked Loop (PLL) structure. The PLL type and dynamics are not deeply affecting the performance of the proposed OBC, so it will not be further discussed here. Several PLL present in the literature are suitable for a reliable grid phase estimation [17].

If required by the TSO, a phase shift $\Delta\varphi$ between grid voltage and reference current can be introduced for generating or absorbing reactive power from the grid. If a unitary PF is required, the reference phase shift $\Delta\varphi$ is set to zero.

B. Zero Torque Through Rotor Parking

The main drawback of the IFI-1ph base solution is that a sinusoidal flux is forced to the machine, possibly producing torque. Two solutions are proposed here to avoid it, namely rotor parking and active zero torque control.

Being the machine under test a PMSM, one solution is to align the rotor with the d axis along the flux generated by the grid excitation (Figure 4(a)). If the grid is connected between the phases b_1 and c_1, this corresponds to align the d axis along β direction. In this way, the machine is naturally excited along the PM direction and no torque is produced. In this case, the a phases of the two 3-phase sets are not connected, as in Figure 4(a), so the current vector will necessarily lay on the β axis. This requires the possibility to align the motor along a specific direction, which may be feasible or not depending on the e-axle topology. It must be considered that most of the modern EV present a transmission gearbox connecting the motor to the wheel shaft, with typical reduction ratio of $8 \div 12$.

As an example, if the gearbox is equipped with a disconnect clutch, this can be used for mechanically separating the rotor and so permitting its freeshaft parking. If the disconnect clutch

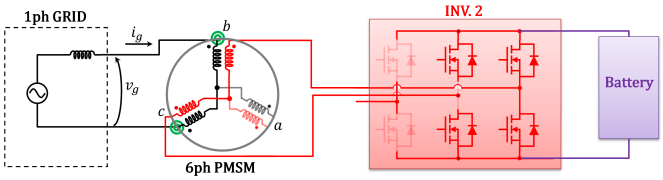

(a)

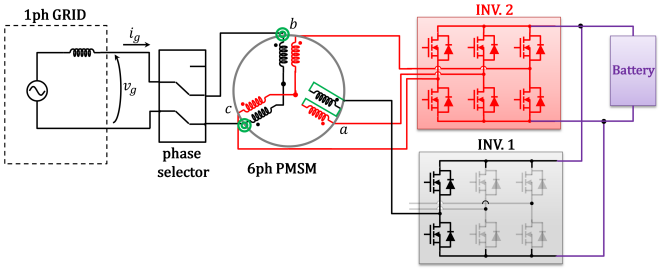

(b)

Fig. 4. Proposed IFI-1ph OBC topology with (a) rotor parking and (b) active zero torque control. With this phase selection: $i_g = i_{b1} = -i_{c1}$, $v_g = v_{bc,1}$, $i_t = i_{a1}$.

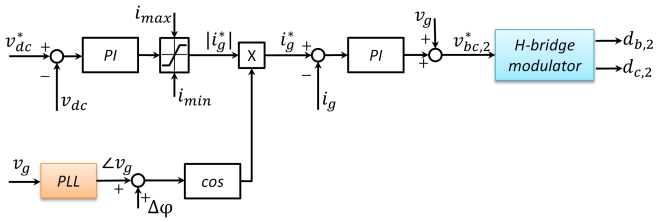

Fig. 5. Block diagram for grid current control for IFI-1ph configuration.

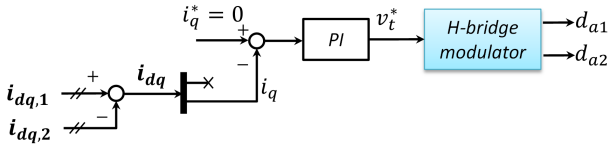

Fig. 6. Block scheme for active zero torque control using dq current control for IFI-1ph configuration.

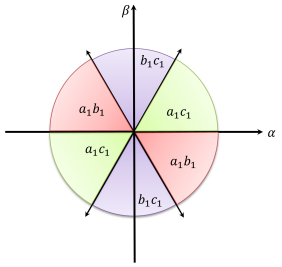

Fig. 7. Scheme for selecting the phases to be connected to the grid in varying the initial rotor position for the IFI-1ph OBC with active zero torque control.

is not present, aligning the d axis along β direction would require a rotation of maximum $\pm 90°$ in electrical coordinates (worst case situation), corresponding to ± 30 mechanical degrees at the rotor shaft. Considering the transmission gearbox, this would produce a rotation of the wheels of $\approx \pm 3°$ and so a linear movement of the car lower than 2 cm.

C. Zero Torque Through Active Zero Torque Control

The second option proposed here is to actively control the torque to be zero whatever the rotor position. In this case, the rotor will not move from its initial position, which is random, without necessarily being locked since no torque is produced. The two phases connected to the grid are selected in such a way that the flux produced by the grid excitation is as close as possible to the d axis. So, the deviation between the magnetizing current and the d axis is minimized. As an example, the grid will be connected between the phases b_1 and c_1 as in Figure 4(b) if the rotor position is between 60° and 120° or between 150° and 210°. If the initial position is between 0° and 60° or between 180° and 240°the single phase grid will be connected between the terminals of the phases a_1 and c_1, thus the excitation flux imposed by the grid grid will have a phase of 30°. Otherwise, the phases a_1 and b_1 will be adopted (grid excitation flux at -30°). The phase selection scheme depending on the rotor position is reported

in Figure 7. In any case, the flux excitation imposed by the grid will not fall in d axis, but it will have a deviation of maximum 30° in the worst case.

The third phase (phase a in the example of Fig. 4(b)), i.e. the one not connected to the grid, will be called "torque phase" and inficated with the subscript t as it is adopted for implementing the active zero torque control. The PMSM is reconfigured from the scheme reported in Figure 4(a) to the one in Figure 4(b). The two star points are open and the torque phase of each set (phases a_1 and a_2 in the example) are connected together. In this way, the phases a_1 and a_2, being in series, will share the same current. Such current is controlled to force zero torque using the correspondent legs of the two inverters as a second H-bridge.

The proposed block diagram for actively controlling $T = 0$ is shown in Figure 6. It exploits a modified current control in dq reference frame. Considering (8), the torque can be forced to zero by imposing the magnetizing current in q axis i_q to be equal to zero, and so also $\lambda_q = 0$. In this way, the magnetizing current vector is aligned with the PM and no torque is produced.

For doing so, the magnetizing current $\boldsymbol{i_{dq}}$ is estimated from (4). Thanks to the choice of the phases as in Figure 7, the torque phase direction is close to the q axis. Therefore, i_q can be forced to zero through a PI regulator, whose output is the reference voltage v_T of the torque phase H-bridge (the voltage between the phases a_1 and a_2 in the example). It should be noted that this is again another non-standard current control, since the applied voltage is not in the direction of the controlled current but it can have a maximum deviation of 30°.

VII. Simulation Results

The proposed IFI OBC was validated by extensive simulations using PLECS software. As said, to avoid excessive core saturation in each test the number of turns is virtually increased by 3 times, assuming the winding configuration of the poles connections is changed from parallel to series.

Figure 8 reports the currents and voltages in the grid side for the 3ph-ISI OBC, controlled according to Figure 3(b). The current THD is ≈5%, and the phase shift between current and voltage is ≈2°, which means PF≈1. As said, this configuration produces relevant shaft torque and requires rotor locking. A solution to this problem is currently under investigation, so the 3-phase case will not be further discussed here.

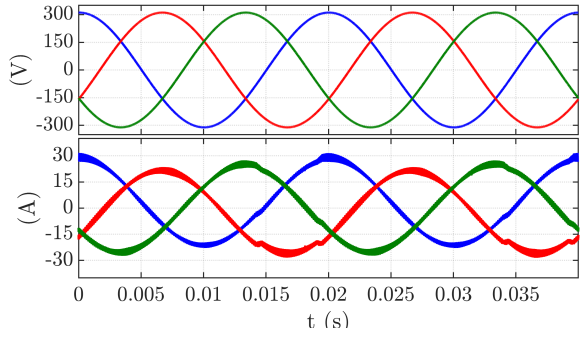

Fig. 8. Grid side voltage and current for three-phase inlet.

For the case of single phase inlet, at first the topology of Figure 4(a) was tested, considering a rotor parking, as in Section VI-B. The rotor position is θ=90°, i.e. the d axis is aligned with β. The rated power 6.7 kW is absorbed from the grid. The results are depicted in Figure 9. The upper subplot shows the grid side voltage and current. Since the grid is connected between the phases b_1 and c_1, the grid voltage corresponds to $v_{bc,1}$ and the grid current is $i_g = i_b = -i_c$. The phase a is not connected, so $i_a = 0$. As can be seen, the current is properly controlled to be in phase with the grid voltage, with PF≈1 and a THD<2.5%. Therefore, the grid constrains [15] are well respected.

The lower plot of the same Figure reports the correspondent voltage and current on the battery side of the PMSM, showing a similar voltage but a higher current and lower PF. This can be explained considering that the PMSM is acting as a transformer, so it has to absorb reactive power for magnetizing the rotor. Since PF=1 on the primary side, such reactive power is given by the secondary side of the machine.

The two subplots of Figure 10 refer again to the current and voltage on the grid and battery side respectively, but in this case the active zero torque control technique described in Section VI-C was adopted instead of rotor parking. The rotor is in the worst case of initial alignment (d axis 30° away from

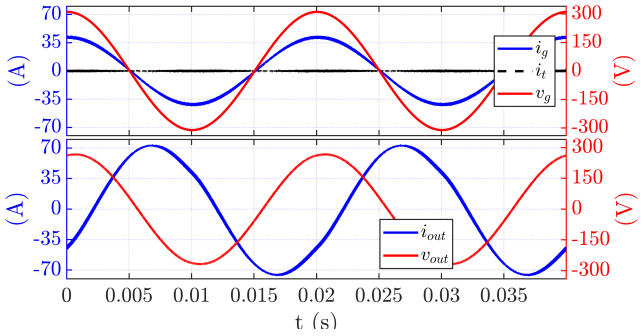

Fig. 9. IFI-1ph using initial parking (θ=90°). Upper plot: current and voltage on grid side of the PMSM. Lower plot: Current and voltage on the battery side.

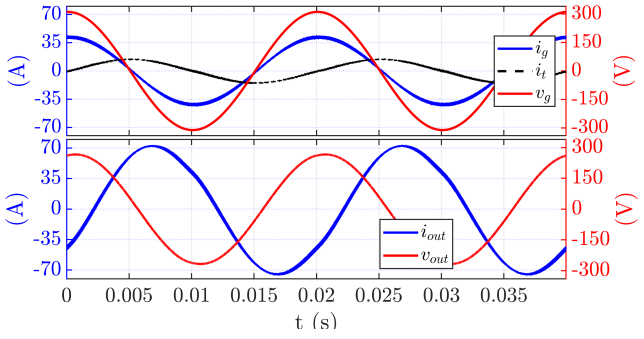

Fig. 10. IFI-1ph using active zero torque control with the worst case of initial position (θ=60°). Upper plot: current and voltage on grid side of the PMSM. Lower plot: Current and voltage on the battery side.

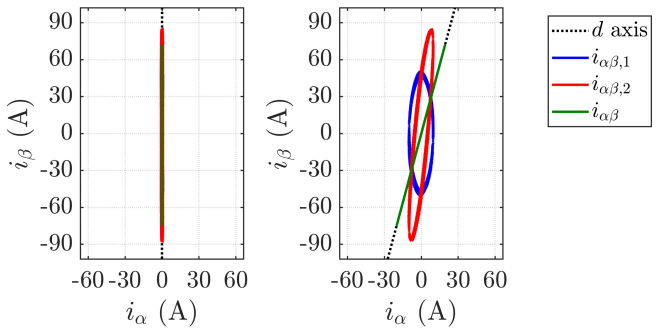

Fig. 11. Trajectories of primary, secondary and magnetizing currents in the $\alpha\beta$ frame with initial parking (left) and with active zero torque control (right).

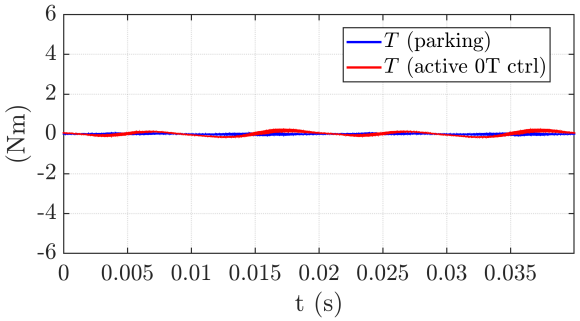

Fig. 12. Shaft torque using initial alignment (blue line) and active zero torque control with the worst case initial position, i.e. 60° (red line).

β axis, i.e. $\theta = 60°$). In terms of i_g, the difference respect to Figures 9 are negligible, since the adopted grid current control is the same (see Section VI-A). In other words, the IFI-1ph OBC is able to properly control the grid current regardless the method adopted for avoiding to produce torque, either free-shaft parking or active zero torque control.

The subplots in Figure 11 show the trajectories of the current vectors $\boldsymbol{i_{\alpha\beta,1}}$, $\boldsymbol{i_{\alpha\beta,2}}$ and the magnetizing current $\boldsymbol{i_{\alpha\beta}}$ in the $\alpha\beta$ plane, again for the IFI-1ph configuration with initial parking and with active zero torque control respectively. In the left subplot, being the a phase disconnected, every current vector moves along β direction, which corresponds to the d axis. In the second subplot, the rotor is 30° shifted from β axis and the phase a is controlled to actively force zero torque through the scheme in Figure 6. Since the grid is still connected between the phases b_1 and c_1, the main excitation is again in β direction. Anyway, in this case the current in a phase deviates the current vectors, so that the magnetizing current $\boldsymbol{i_{\alpha\beta}}$ falls on the d axis.

Finally, Figure 12 shows the torque when adopting the free-shaft parking (blue) or with active zero torque control (red). In both cases the proposed techniques work very well, as negligible torque is obtained. It should be remarked that without one of the two techniques, the torque at the shaft would be very high.

Overall, the 1-ph results are promising, demonstrating effective charging capability without torque production.

Conclusions

This work proposes an integrated battery charger for EVs with 6-phase traction drive, where the PMSM is working as transformer, thus providing galvanic insulation between grid and battery sides, not guaranteed by existing integrated solutions. Appropriate control techniques for regulating the charging power, grid current PF and THD have been developed. Moreover, for the case of single phase inlet two methods for avoiding to produce torque during charging were presented. Extensive simulation results confirm the proposed solution is promising, with good charging control capability.

Acknowledgments

The authors are grateful to the European Commission for the support to the present work, performed within the EU H2020 project FITGEN (Grant Agreement 824335).

References

[1] European Roadmap Electrification of Road Transport, 3rd Edition, Version: 10, June 2017.
[2] A. Salem and M. Narimani, "A Review on Multiphase Drives for Automotive Traction Applications," in IEEE Transactions on Transportation Electrification, vol. 5, no. 4, pp. 1329-1348, Dec. 2019.
[3] De Gennaro Michele et Al., "The H2020 project FITGEN: preliminary results and design guidelines of an integrated e-axle for the third-generation electric vehicles," in *Transport Research Arena (TRA2020)*, 2020, Helsinki (Finland).
[4] A. Khaligh and S. Dusmez, "Comprehensive Topological Analysis of Conductive and Inductive Charging Solutions for Plug-In Electric Vehicles," in IEEE Trans. on Vehicular Technology, Oct. 2012.
[5] L. Solero, "Nonconventional on-board charger for electric vehicle propulsion batteries," in *IEEE Transactions on Vehicular Technology*, vol. 50, no. 1, pp. 144-149, Jan. 2001.
[6] A. Bruyère, L. De Sousa, B. Bouchez, P. Sandulescu, X. Kestelyn and E. Semail, "A multiphase traction fast-battery-charger drive for electric or plug-in hybrid vehicles: Solutions for control in traction mode," 2010 IEEE Vehicle Power and Propulsion Conference, Lille, 2010, pp. 1-7.
[7] G. Pellegrino, E. Armando and P. Guglielmi, "An Integral Battery Charger With Power Factor Correction for Electric Scooter," in *IEEE Transactions on Power Electronics*, vol. 25, no. 3, pp. 751-759, 2010.
[8] S. Lacroix, E. Laboure and M. Hilairet, "An integrated fast battery charger for Electric Vehicle," 2010 IEEE Vehicle Power and Propulsion Conference, Lille, 2010, pp. 1-6.
[9] US Patent 2012/028674.0 A1.
[10] I. Subotic, N. Bodo and E. Levi, "Single-Phase On-Board Integrated Battery Chargers for EVs Based on Multiphase Machines," in *IEEE Transaction on Power Electronics*, 2016.
[11] I. Subotic, N. Bodo, E. Levi, B. Dumnic, D. Milicevic and V. Katic, "Overview of fast on-board integrated battery chargers for electric vehicles based on multiphase machines and power electronics," in IET Electric Power Applications, vol. 10, no. 3, pp. 217-229, 3 2016.
[12] M. Yilmaz and P. T. Krein, "Review of Battery Charger Topologies, Charging Power Levels, and Infrastructure for Plug-In Electric and Hybrid Vehicles," in IEEE Transactions on Power Electronics, vol. 28, no. 5, pp. 2151-2169, May 2013.
[13] F. Barrero and M. J. Duran, "Recent Advances in the Design, Modeling, and Control of Multiphase Machines—Part I," in *IEEE Transactions on Industrial Electronics*, Jan. 2016.
[14] P. Xu, J. H. Feng, S. Y. Guo, S. Feng, W. Chu, Y. Ren, Z. Q. Zhu, "Analysis of Dual Three-Phase Permanent-Magnet Synchronous Machines With Different Angle Displacements," in *IEEE Trans. on Industrial Electronics*, vol. 65, no. 3, pp. 1941-1954, 2018.
[15] International standard IEC 61851-1:2017-02
[16] M. C. Kisacikoglu, M. Kesler and L. M. Tolbert, "Single-Phase On-Board Bidirectional PEV Charger for V2G Reactive Power Operation," in IEEE Transactions on Smart Grid, vol. 6, no. 2, pp. 767-775, 2015.
[17] Remus Teodorescu, Marco Liserre, Pedro Rodriguez, "Grid Synchronization in SinglePhase Power Converters," in *Grid Converters for Photovoltaic and Wind Power Systems* , IEEE, 2007, pp.43-91.